

# Measuring Cosmic Density of Neutral Hydrogen via Stacking the DINGO-VLA Data

Qingxiang Chen,<sup>1,2\*</sup> Martin Meyer,<sup>1,3</sup> Attila Popping,<sup>1,2</sup> Lister Staveley-Smith,<sup>1,3</sup> Julia Bryant,<sup>3,4,5</sup> Jacinta Delhaize,<sup>6</sup> B. W. Holwerda,<sup>7</sup> M. E. Cluver,<sup>8,9</sup> J. Loveday,<sup>10</sup> Angel R. Lopez-Sanchez,<sup>3,11,12</sup> Martin Zwaan,<sup>13</sup> E. N. Taylor,<sup>8</sup> A. M. Hopkins,<sup>11</sup> Angus Wright,<sup>14</sup> Simon Driver,<sup>1,15</sup> S. Brough<sup>16</sup>

<sup>1</sup>The International Centre for Radio Astronomy Research (ICRAR), University of Western Australia, 35 Stirling Hwy, Crawley, WA 6009, Australia

<sup>2</sup>ARC Centre of Excellence for All-sky Astrophysics (CAASTRO)

<sup>3</sup>ARC Centre of Excellence for All Sky Astrophysics in 3 Dimensions (ASTRO 3D)

<sup>4</sup>Australian Astronomical Optics, AAO-USydney, School of Physics, University of Sydney, NSW 2006, Australia

<sup>5</sup>Sydney Institute for Astronomy (SIfA), School of Physics, Faculty of Science, The University of Sydney, NSW 2006, Australia

<sup>6</sup>Department of Astronomy, University of Cape Town, Private Bag X3, Rondebosch 7701, South Africa

<sup>7</sup>Department of Physics and Astronomy, 102 Natural Science Building, University of Louisville, Louisville KY 40292, USA

<sup>8</sup>Centre for Astrophysics and Supercomputing, Swinburne University of Technology, John Street, Hawthorn, 3122, Australia

<sup>9</sup>Department of Physics and Astronomy, University of the Western Cape, Robert Sobukwe Drive, Bellville, 7535, South Africa

<sup>10</sup>Astronomy Centre, University of Sussex, Falmer, Brighton BN1 9QH, UK

<sup>11</sup>Australian Astronomical Optics, Macquarie University, 105 Delhi Rd, North Ryde, NSW 2113, Australia

<sup>12</sup>Department of Physics and Astronomy, Macquarie University, NSW 2109, Australia

<sup>13</sup>European Southern Observatory, Karl-Schwarzschildstrasse 2, D-85748 Garching bei München, Germany

<sup>14</sup>Ruhr-Universität Bochum, Astronomisches Institut, German Center for Cosmological Lensing, Universitätsstr 150, 44780, Bochum, Germany

<sup>15</sup>School of Physics & Astronomy, University of St Andrews, North Haugh, St Andrews KY16 9SS, UK

<sup>16</sup>School of Physics, University of New South Wales, NSW 2052, Australia

Last updated 2016 Nov 17

## ABSTRACT

We use the 21 cm emission line data from the DINGO-VLA project to study the atomic hydrogen gas H I of the Universe at redshifts  $z < 0.1$ . Results are obtained using a stacking analysis, combining the H I signals from 3622 galaxies extracted from 267 VLA pointings in the G09 field of the Galaxy and Mass Assembly Survey (GAMA). Rather than using a traditional one-dimensional spectral stacking method, a three-dimensional cubelet stacking method is used to enable deconvolution and the accurate recovery of average galaxy fluxes from this high-resolution interferometric dataset. By probing down to galactic scales, this experiment also overcomes confusion corrections that have been necessary to include in previous single dish studies. After stacking and deconvolution, we obtain a  $30\sigma$  H I mass measurement from the stacked spectrum, indicating an average H I mass of  $M_{\text{H I}} = (1.674 \pm 0.183) \times 10^9 M_{\odot}$ . The corresponding cosmic density of neutral atomic hydrogen is  $\Omega_{\text{H I}} = (0.377 \pm 0.042) \times 10^{-3}$  at redshift of  $z = 0.051$ . These values are in good agreement with earlier results, implying there is no significant evolution of  $\Omega_{\text{H I}}$  at lower redshifts.

**Key words:** galaxies: star formation, radio lines: galaxies, ISM: atoms

## 1 INTRODUCTION

Following decades of effort, the evolution of the cosmic star formation rate has been well measured for redshifts  $z < 3$ . It is now known that the star formation rate density has dropped by more than an order of magnitude since  $z \sim 1$  (Lilly et al. 1996; Madau et al. 1996; Hopkins 2004; Hopkins & Beacom 2006; Hopkins et al.

2008; Madau & Dickinson 2014). In contrast, less is known about how the cold gas content of galaxies has evolved during the same cosmic period (e.g. Meyer et al. 2004; Giovanelli et al. 2005; Giovanelli & Haynes 2015). Since cold gas is the fuel for future star formation, understanding its availability via observations and theory is essential for the development of a holistic picture of the physics of galaxy formation and evolution.

Much effort has been expended in developing models which relate the physical mechanisms responsible for the accretion and

\* E-mail: chenqingxiangcn@gmail.com

outflow of gas, and the collapse of cold gas clouds in galaxies over cosmic time, and the identification of the major physical mechanisms (e.g. Lagos et al. 2018). There are many models dealing with different physical mechanisms at a variety of spatial and mass scales, such as the complex gas dynamics of AGN and supernova feedback (e.g. Somerville et al. 2001; Cen et al. 2003; Nagamine et al. 2005; Power et al. 2010; Lagos et al. 2011). As such, observational measurements and constraints are becoming even more crucial.

At high redshifts, the damped Lyman- $\alpha$  absorption systems (DLAs) are often used as a tracer of neutral atomic hydrogen gas. Using spectroscopic data from the Sloan Digital Sky Survey (SDSS), the H I cosmological mass density can be measured at  $z > 2$  (e.g. Prochaska et al. 2005; Prochaska & Wolfe 2009). These results may contain systematic biases due to dust extinction (e.g. Ellison et al. 2001; Jorgenson et al. 2006) and gravitational lensing (e.g. Smette et al. 1997). At  $z < 1.6$ , Lyman- $\alpha$  enters the ultra-violet regime, and becomes hard to detect using ground-based telescopes. In the local Universe, on the other hand, the preferred method to trace H I is to directly observe the 21-cm emission line of atomic hydrogen. Thanks to large 21-cm emission line blind surveys, the neutral hydrogen mass function and density have been precisely measured in the local Universe at  $z \sim 0$  (Zwaan et al. 2005; Martin et al. 2010; Jones et al. 2018). However, beyond the local Universe, direct detection of H I is very challenging due to the relative weakness of the H I signal compared to the sensitivity of existing observing facilities. Deep blind surveys, such as the Arecibo Ultra-Deep Survey (AUDS, Hoppmann et al. 2015), the Blind Ultra-Deep H I Environmental Survey (BUDHIES, Gogate et al. 2020) and the COSMOS H I Large Extragalactic Survey (CHILES, Fernández et al. 2013; Hess et al. 2019) are able to probe higher redshift H I, but require extremely long integration times. At certain redshifts, where the signal falls outside the protected radio astronomy band, the impact of radio frequency interference (RFI) can also severely limit sensitivity (e.g. Fernández et al. 2016).

Thus, there are still considerable uncertainties in our understanding of H I evolution at  $z > 0.1$ , and therefore the relationship between H I gas content and the dramatic decrease of the star formation rate density. The next generation of radio telescopes such as the Australian Square Kilometre Array Pathfinder (ASKAP, DeBoer et al. 2009), the Meer-Karoo Array Telescope (MeerKAT, Jonas 2009) and ultimately the Square Kilometre Array (SKA, Carilli & Rawlings 2004) will likely tackle these problems with their better sensitivity and larger field-of-view. Other than developing these instruments, a technique involving the co-adding of signals from hundreds or thousands of galaxies whose H I signals are too weak to detect directly, has been developed. It was first introduced by Zwaan (2000), and later by Chengalur et al. (2001), probing the gas content of cluster galaxies. Using this technique, the cosmic density of neutral hydrogen can be measured to higher redshifts using single-dish radio telescopes, such as the Parkes telescope, and interferometers such as the Westerbork Synthesis Radio Telescope (WSRT) and the Giant Metrewave Radio Telescope (GMRT) (e.g. Delhaize et al. 2013; Rhee et al. 2013; Hu et al. 2019; Lah et al. 2007, 2009; Rhee et al. 2016, 2018; Bera et al. 2019; Chowdhury et al. 2020).

In this paper we develop and apply a new H I stacking method for the Karl G. Jansky Very Large Array (VLA) pathfinder project of the ASKAP Deep Investigation of Neutral Gas Origin survey (DINGO, Meyer 2009). This method overcomes observational limitations due to the poor  $uv$ -coverage of short observations, and the subsequent non-Gaussian synthesised beam and large sidelobes.

Such limitations make it hard to apply the traditional spectral stacking technique when sources are partially resolved. The new method (*Cubelet Stacking*) solves this problem. Instead of extracting and stacking spectra, we stack small cubelet cut-outs from the area centered on the known galaxy positions. Then we deconvolve the stacked cubelets using a stacked point spread function and extract a spectrum from this stacked cube. For more information on this stacking technique, readers are recommended to read Chen et al. (2021) (hereafter: Paper I).

The paper is organised as follows. Section 2 introduces the optical and radio data used in this work. Section 3 presents our radio data reduction pipeline. In Section 4 we present the sample, summarise the stacking method and show the results. The H I cosmic density is calculated in Section 5, followed by a summary and conclusions in Section 6. We adopt the concordance cosmological parameters of  $\Omega_\Lambda = 0.7$ ,  $\Omega_M = 0.3$ , and  $H_0 = 70 \text{ km s}^{-1} \text{ Mpc}^{-1}$  and use Loveday et al. (2012) for the optical luminosity function and density for our analysis.

## 2 DATA

This section introduces both the optical and H I data used in this work. For the analysis of our data we are using an H I stacking technique, as the H I emission lines from most galaxies in our sample are too faint to detect directly. An optical input catalogue providing the positions and redshifts of galaxies is used as a prior to locate the likely position of signal in the H I data.

### 2.1 Optical Data

The optical input catalogues used in this work are from the Galaxy And Mass Assembly survey (GAMA, Driver et al. 2011; Hopkins et al. 2013; Liske et al. 2015). GAMA is a multi-wavelength galaxy survey covering several regions of the sky. In this study we only focus on the G09 field covering the RA range between  $129^\circ$  and  $141^\circ$  and the DEC range from  $-2^\circ$  to  $+3^\circ$ . One of the core components of GAMA is a large spectroscopic redshift survey carried out with 2dF/AAOmega on the Anglo-Australian Telescope (AAT). This survey observed  $\sim 300,000$  galaxies with  $r < 19.8$  mag over  $\sim 286 \text{ deg}^2$ . The G09 catalogue includes coordinates, redshifts, distances, dust extinctions and magnitudes of galaxies from the GAMA 3rd data release (Baldry et al. 2018). The area of this region is  $\sim 60 \text{ deg}^2$  and the magnitude limit is  $r < 19.8$ .

The G09 input redshifts used in this paper are from the combined catalog SpecALL, which combined redshifts from the GAMA AAT spectroscopic observations and other publicly available catalogues including SDSS/BOSS DR10 (Ahn et al. 2014), 6dF Galaxy Survey (Jones et al. 2009), 2dF SDSS LRG and QSO survey (Canon et al. 2006; Croom et al. 2009), WiggleZ Dark Energy Survey (Parkinson et al. 2012) and Updated Zwicky Catalog (Falco et al. 1999). The redshift quality is encoded by  $NQ$  (1 – 4), ranked from failure to most confident. Throughout this paper we select galaxies with secure redshifts with  $NQ > 2$ . The overall completeness of secure redshifts in G09 is 98.48% at  $r < 19.8$ . Interested readers are referred to Liske et al. (2015) and Baldry et al. (2014) for extensive discussions on how these redshifts are measured and categorized. Also, in order to avoid confusion with star-like objects, galaxies with a heliocentric redshift below 0.002 are not considered. We use two different types of GAMA redshifts (Baldry et al. 2018): heliocentric redshifts are used to determine the location of galaxies in the radio data. To calculate luminosity distances, we use

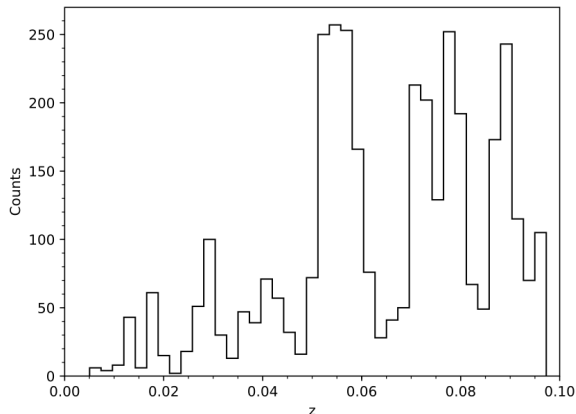


**Figure 1.** The redshift distribution of the 3622 galaxies with  $z < 0.1$  stacked in this work. These are CMB redshifts corrected for local flow.

the CMB redshifts corrected for the local flow model of [Tonry et al. \(2000\)](#). The redshift error is only  $27 \text{ km s}^{-1}$  and should not affect our stacking analysis. It should slightly smear out flux along the frequency axis of our stacked cubes, but conserve it. Therefore we do not consider redshift errors in this work.

The  $u, g, r, i, z$  luminosity functions and densities of the G09 galaxies are provided in [Loveday et al. \(2012\)](#). For this study, we only use the luminosity function in the  $r$ -band as it has the highest accuracy. All magnitudes in the catalogues were adjusted for effects due to dust extinction and  $k$ -correction. For this paper, we limit the redshift to the RFI-free redshift range  $z < 0.1$ . A later study will examine data at higher redshifts. We match the optical data with the sky area of VLA data, resulting in a total galaxy sample of 7146. After considering further observational constraints, selecting only galaxies with positions within the VLA primary beam, and selecting only galaxies which have data extending  $\pm 2$  MHz from the redshifted  $\text{H I}$  frequency, the number of galaxies in the sample decreases to 3622. Fig. 1 shows the redshift distribution of the total sample. This galaxy sample was then used to generate 5442 cubelets to co-add, larger than the number of sample galaxies due to some galaxies appearing in multiple pointings (see Fig. 2).

## 2.2 Radio Observations and Data Reduction

The radio data is obtained from the DINGO-VLA project observed in the 2014B and 2016A semester with the Jansky Very Large Array (VLA). The observations were taken in the C or CnB configurations.

The DINGO-VLA observations include three target pointings and two calibrators within each two-hour scheduling block. The sky positions of the different target pointings are shown in Fig. 2. The complete area of 276 pointings consists of 92 2-hr observing units. In each observing unit the flux density and bandpass calibrator 3C 138 is observed first, followed by the phase calibrator, then the three target pointings. The observation sequence in one observing unit is: flux calibrator,  $4\times$  (phase calibrator  $\rightarrow$  pointing 1  $\rightarrow$  2  $\rightarrow$  3), phase calibrator. Observations of pointings are broken into small intervals to maximize the UV coverage. Each pointing target was observed for a total of 28 mins. The full width half power

(FWHP) circle radius of VLA primary beam at 1.4 GHz is  $\sim 31'$ , resulting in  $\sim 38 \text{ deg}^2$  total survey area.

The correlator of the VLA splits the bandwidth into spectral windows. In this paper we consider the 4 spectral windows which cover the frequency range from 1296 to 1424 MHz, denoted as  $spw8, spw9, spw10, spw11$ . Each  $spw$  spans 32 MHz, with a channel width of 20.833 kHz. Both edges of each spectral window are noisy because of the bandpass response. In order to deal with this problem, another 4 spectral windows are overlaid across the boundaries of the  $spws$ . These four narrow spectral windows are denoted  $spw19, spw20, spw21, spw23$ . Each of them spans 8 MHz and their channel width is 15.625 kHz. We show the 8 spectral windows' frequency coverage in Fig. 3. The frequency range after adding the 4 narrow spectral windows becomes 1292 to 1424 MHz. This strategy significantly improves the data quality and ensures a more uniform rms level over the full frequency range.

We developed a data reduction pipeline for DINGO-VLA based on standard tasks in Common Astronomy Software Applications (CASA, [McMullin et al. 2007](#)). The pipeline was tuned specifically for the the data properties and the large data volume (raw data in measurement set format is larger than 16 TB). Scripts were developed to implement the pipeline in a cluster environment. An outline of the data reduction procedure is in Fig. 4. It includes pre-processing, visibility processing (flagging and calibration), and an imaging step.

First, a pre-processing step is carried out. This includes application of online flags (data taken when not on source or when there were sub-reflector issues), flagging of zero-amplitude data, flagging of auto-correlations, flagging of shadowed antennas, first scan flagging (telescope setup), and so-called quack flagging (the first 10-15s of data are not useful). In addition, we correct for antenna position errors and antenna shape variation (task: *genical*).

The main bandpass and flux density calibrator is 3C 138. This is used to solve for amplitude and phase variations as a function of frequency for all antennas. The second calibrator is used to correct for the complex gain variations (i.e., amplitude and phase) as a function of time. Due to some frequency ranges being affected by RFI, calibration and flagging was applied iteratively. A 2-D automated algorithm (rFlag) was used to flag  $5\text{-}\sigma$  outliers in the time-frequency plane. Strong RFI signals ( $>20 \text{ Jy}$ ) were flagged. Channels and time ranges were completely flagged where more than 80% and 50% of the time or frequency series were flagged, respectively. The calibration procedure was then repeated for more accurate solutions.

We then apply the calibration solutions (bandpass, gain and flux scale) to the three target fields. Again, we use the rFlag algorithm to flag bad data on the 2-D plane. To assist rFlag, we apply a  $3\text{-}\sigma$  clip based on the standard deviation of amplitude across the spectral window beforehand. After rFlag we carry out an extend mode flagging: completely flag target data in each channel / time chunk where more than 50% has already been flagged on the 2-D plane; if there are more than 4 surrounding data points flagged on the 2-D plane, this data point is further flagged.

Finally we carry out the imaging processes. The weighting scheme used is 'robust' ([Briggs 1995](#)) with a robust parameter of 0.8. This value was found to be the optimal compromise between resolution and sensitivity for DINGO-VLA. For every target field, we first obtain the continuum image by carrying out multi-frequency synthesis (MFS) mode imaging ([Rau & Cornwell 2011](#)). The size of each continuum image is 2048 pixels  $\times$  2048 pixels, with the pixel size being  $2'' \times 2''$ . We calculate the rms over all the pixels in the dirty image and deconvolve down to a threshold of

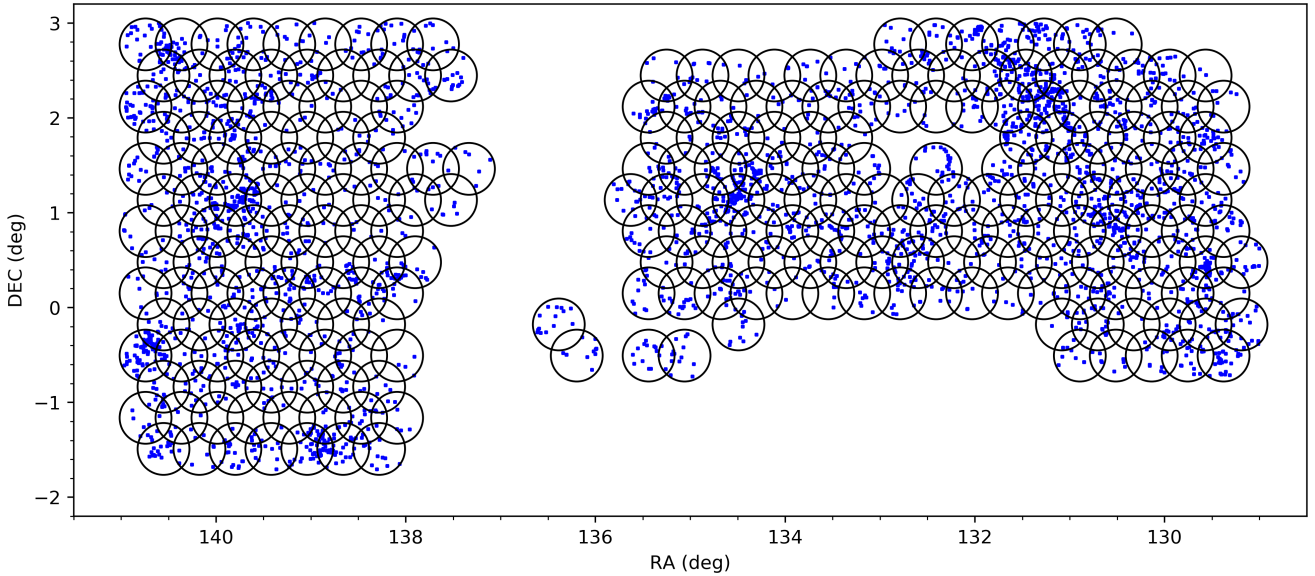


**Figure 2.** The mosaic of pointings of the DINGO-VLA project (circles) from which the radio data used for this work were obtained. The total number of pointings is 267. Each circle indicates one VLA primary beam with a radius of 16.4 arcmin. This approximates the full-width at half power (FWHP) at the frequency corresponding to redshift 0.1. The blue points within circles indicate the positions of the 3622 GAMA galaxies considered in this paper.

5 times this value. Then we subtract the MFS CLEAN source model from the visibilities, and further subtract the continuum residual by directly fitting the real and imaginary visibility data with linear functions in the frequency domain. The four narrow spectral windows (*spw19*, *spw20*, *spw21*, *spw23*) have channel widths of 15.625 kHz, while the four wide spectral windows (*spw8*, *spw9*, *spw10*, *spw11*) have channel widths of 20.833 kHz. We average 4 and 3 channels for narrow and wide spectral windows respectively, to obtain the same channel width (62.5 kHz). We use the re-binned data for the subsequent analysis. Dirty data cubes are made for each spectral window, and concatenated, discarding the duplicate 1 MHz chunks at both edges of each wide spectral window. Every field then has a single data cube consisting of 1024 pixels  $\times$  1024 pixels  $\times$  2048 channels. The pixel size and channel width is 2''  $\times$  2'' and 62.5 kHz respectively.

For every spectral window we chop 2 MHz at both edges so that the spectral windows are aligned. This also changes the overall frequency range for science use. The final visibility data after reduction covers 128 MHz from 1294 to 1422 MHz (more details can be found in next section). The predicted and measured noise behaviour as a function of frequency for a typical field is shown in Fig. 5. The measured rms is obtained directly from the final data cube, and the predicted rms uses the VLA online exposure calculator<sup>1</sup>, taking into account the flagging ratio, the spectral resolution, the configuration, weighting scheme and integration time. The average measured rms is 1.65 mJy beam<sup>-1</sup>, which is within 20% of the predicted value.

<sup>1</sup> <https://obs.vla.nrao.edu/ect>.

### 3 CUBELET STACKING

As discussed in Paper I, traditional stacking methods are not well-suited to interferometric data. The equatorial location of the observations and short integration times lead to significant power in the wings of the PSF, or dirty beam. Combined with the extended nature of some input sources compared to the size of the PSF, this has the potential to lead to significant flux errors. We therefore use the *Cubelet Stacking* technique, first extracting and stacking sub-cubes centred on the known galaxy redshifts and positions, then deconvolving the stacked cube. We then analyse H I mass and density using the spectrum extracted from the clean cube. For more details of the stacking method please refer to Paper I.

#### 3.1 Stacking Sample Selection

A number of selection criteria are applied in extracting the H I data cubelets from the reduced VLA spectral-line observations, as detailed below:

- (i) Only GAMA sources that fall within the full width half maximum (FWHM) of the primary beam for each pointing are extracted.
- (ii) Sources for which we cannot extract a 200 pixels  $\times$  200 pixels region (400''  $\times$  400''), centred on the position of the GAMA galaxy, are omitted.
- (iii) Each cubelet should be at least 4 MHz wide along the frequency axis, centred on the frequency of the 21-cm line (1420.406 MHz), after aligning the cubelet to the rest frame. This is to avoid spectra with only partial frequency information. Due to the observed frequency range of 1294 to 1422 MHz, this excludes galaxies with redshifts  $z > 0.095$ . There are some completely flagged channels within the central 4 MHz for some of the



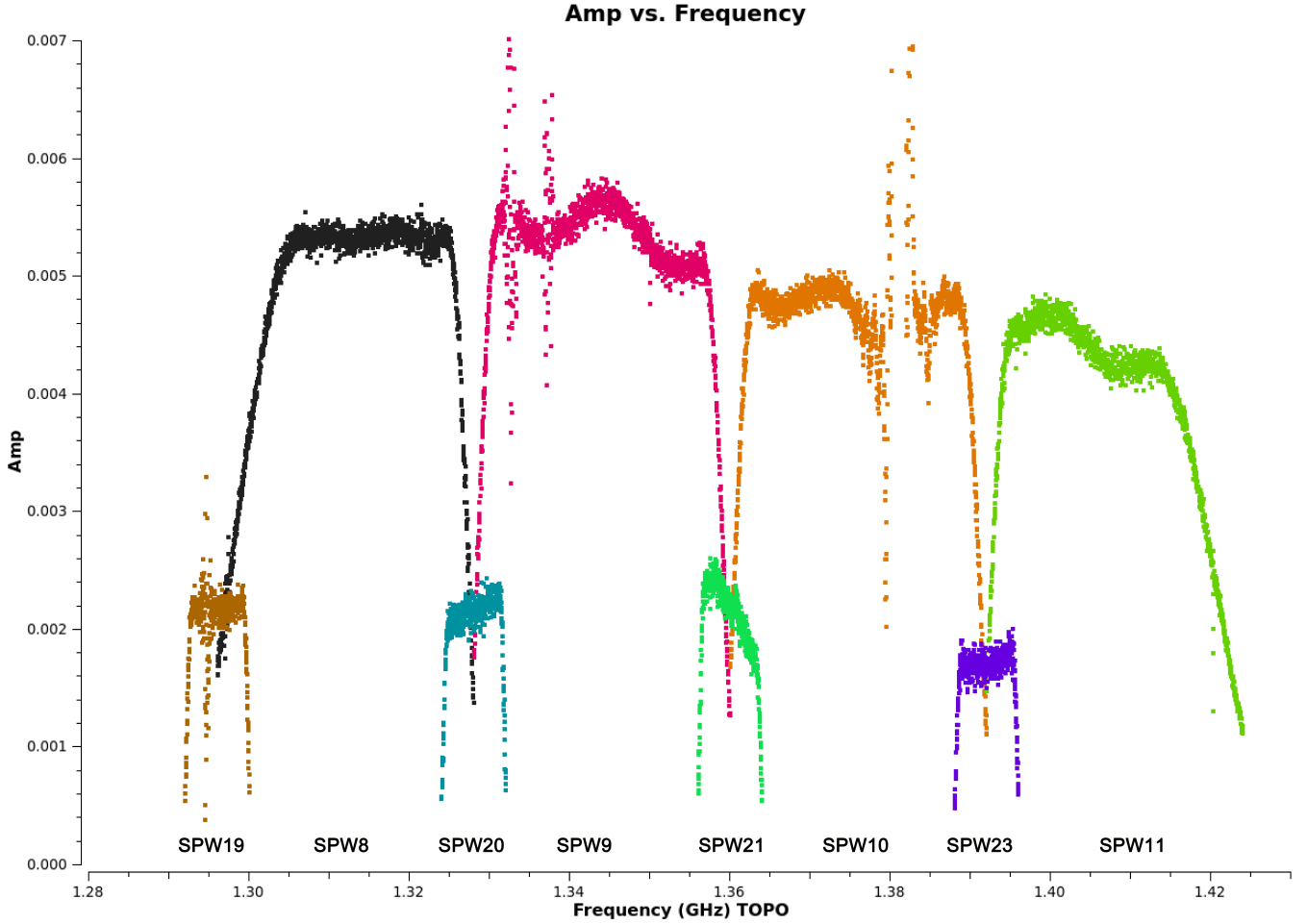


**Figure 3.** A plot of amplitude against frequency showing the layout of four wide 32-MHz spectral windows of the VLA correlator used in this analysis (*spw8*, *spw9*, *spw10*, *spw11*), and the four narrow 8-MHz spectral windows (*spw19*, *spw20*, *spw21*, *spw23*) positioned to fill the subsequent gaps. Here we plot the bandpass calibrator raw data from a randomly chosen observing unit after averaging along polarisation, time and uv-distance axes. The channel width in the wide and narrow windows is 20.833 and 15.625 kHz, respectively.

cubelets. They are included in this sample, but given zero weight in the stacking process.

(iv) The redshift quality flag (NQ) in the GAMA optical catalogues is larger than 2.

Applying the above criteria yields a sample of 3622 galaxies for stacking. Due to some galaxies being covered in adjacent pointings, there are a total of 5442 cubelets. Fig. 1 shows the redshift distribution of the sample.

### 3.2 Stacking Methodology

Following extraction of each  $400'' \times 400'' \times 4$  MHz cubelet centred on the optical position and redshift from GAMA, a corresponding  $200 \times 200$  pixel PSF cubelet is also extracted from the centre of the PSF cube generated by the pipeline for each observation. These are used for stacking as described below.

(i) *Primary Beam Correction.* For each image cubelet, we calculate the distance to the pointing centre of the observation, and

calculate the primary beam correction factor for this cubelet based on its position using the VLA primary beam response:

$$f = a_0 + a_1 X^2 + a_2 X^4 + a_3 X^6, \quad (1)$$

where  $X = \nu\theta$  where  $\theta$  is the angle between the source and pointing centre in arcmin, and  $\nu$  is the observation frequency in GHz. The four coefficients are provided in Perley (2016): 1.000,  $-1.428 \times 10^{-3}$ ,  $7.62 \times 10^{-7}$ ,  $-1.54 \times 10^{-10}$  at 1296 MHz; 1.000,  $-1.449 \times 10^{-3}$ ,  $8.02 \times 10^{-7}$ ,  $-1.74 \times 10^{-10}$  at 1360 MHz and 1.000,  $-1.462 \times 10^{-3}$ ,  $8.23 \times 10^{-7}$ ,  $-1.83 \times 10^{-10}$  at 1424 MHz. Responses at intermediate frequencies are derived by linearly interpolation. A primary beam correction is applied to each image cubelet by dividing pixel values with the primary beam response  $f$ . To limit the point spread function variance and enhance the chances of successful deconvolution, we apply the same primary beam correction to all pixels in the cubelet.

(ii) *Blueshifting to the rest frame.* Each image cubelet and corresponding PSF cubelet is shifted to rest frame using the optical redshift:

$$\nu_{\text{rest}} = \nu_{\text{obs}}(1 + z), \quad (2)$$

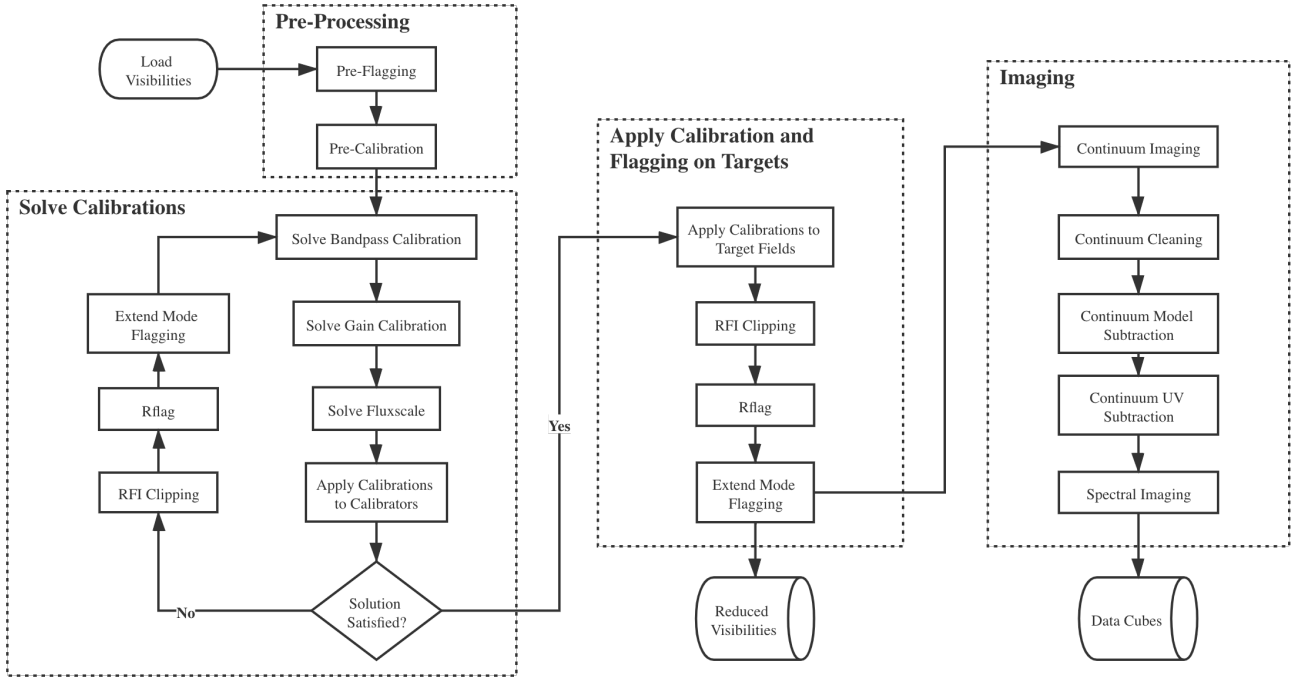


**Figure 4.** An illustrative flow-chart of the data reduction procedures for DINGO-VLA. A more detailed description of the pipeline is in Section 2.2.

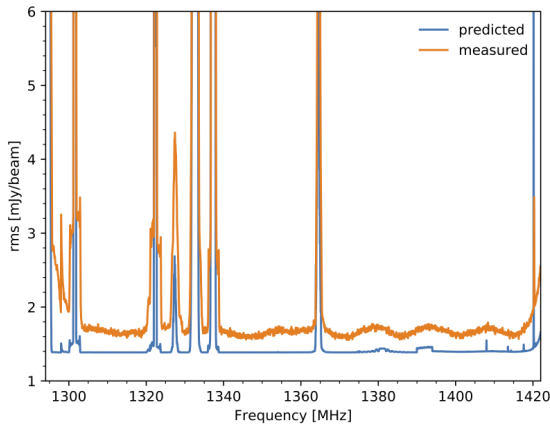


**Figure 5.** The measured and predicted rms as a function of frequency for a typical field. The orange line is the rms level directly measured from the reduced data cube. The blue line is the predicted rms level. The latter is calculated by scaling the prediction from the VLA online Exposure calculator, taking into account the flagging fraction. The channel width in this measurement is 62.5 kHz.

where  $\nu_{\text{rest}}$  and  $\nu_{\text{obs}}$  are the rest frame and observation frame frequency, respectively. To ensure flux is conserved after blueshifting, the image cubelet pixel values  $S_{ij}(\nu_{\text{obs}})$  are also scaled with redshift to  $S_{ij}(\nu_{\text{rest}})$  as follows:

$$S_{ij}(\nu_{\text{rest}}) = \frac{S_{ij}(\nu_{\text{obs}})}{(1+z)} \quad (3)$$

(iii) *Conversion to mass density.* For each image cubelet we convert every pixel from flux units ( $\text{Jy beam}^{-1}$ ) to  $\text{H I}$  mass ( $M_{\odot} \text{ beam}^{-1}$ ) using (Meyer et al. 2017):

$$\frac{M_{\text{HI}}'(\nu)}{M_{\odot} \text{ beam}^{-1} \text{ channel}^{-1}} = 49.7 \left( \frac{D_L}{\text{Mpc}} \right)^2 \left( \frac{S(\nu) \cdot \Delta f}{\text{Jy beam}^{-1} \text{ Hz}} \right) \quad (4)$$

In this equation,  $D_L$  is the luminosity distance calculated using the cosmological parameters given in Section 1, and  $\Delta f$  is the frequency channel spacing after blueshifting. Note that after this step, the image cubelet pixels are in units of  $M_{\odot} \text{ beam}^{-1} \text{ channel}^{-1}$ .

(iv) *Frequency interpolation.* We interpolate all the image and PSF cubelets to have the same rest-frame channelisation of  $160 \times 62.5$  kHz (10 MHz), each channel being 62.5 kHz ( $13.2 \text{ km s}^{-1}$ ) in order to facilitate combination. This provides enough channels for baseline fitting and subtraction after extracting the spectrum.

(v) *Weighting.* For each image cubelet and corresponding PSF cubelet, we calculate the weight in each channel from:

$$w_i = \sigma_i^{-2} D_L^{\gamma}, \quad (5)$$

where  $\sigma_i$  is the rms for each channel, and  $D_L$  is the luminosity distance. The rms noise is calculated from the corresponding channel in the original data cube. The distance index  $\gamma (\leq 0)$  is introduced as a parameter that can be adjusted to emphasise nearby galaxies (for good S/N ratio, for example), or to emphasise distant galaxies (for lower cosmic variance, for example).

(vi) *Stacking image and PSF cubelets.* We co-add the image and PSF cubelets channel-by-channel using:

$$M_{ij}(\nu_{\text{grid}}) = \frac{\sum_l M_{ijl}(\nu_{\text{grid}}) w_l(\nu_{\text{grid}})}{\sum_l w_l(\nu_{\text{grid}})}, \quad (6)$$

and

$$P_{ij}(v_{\text{grid}}) = \frac{\sum_l P_{ijl}(v_{\text{grid}})w_l(v_{\text{grid}})}{\sum_l w_l(v_{\text{grid}})} \quad (7)$$

For each cubelet, empty channels are given zero weight, but normal channels are not affected.

(vii) *Deconvolution.* We deconvolve the stacked image cubelets using the stacked PSF cubelet. Note that this is purely done in the image domain using the *CASA* task *deconvolve*. Following Paper I we implement a Högbom CLEAN with a multi-scale parameter of [6 pix, 12 pix, 18 pix], a central circular cleaning mask of radius  $20''$ , and CLEAN down to  $1-\sigma$ , where  $\sigma$  is calculated from all pixels, excluding the central 33 channels (3.0625 MHz) where we expect H I. The deconvolved image is restored with a two dimensional Gaussian function fitted to the stacked PSF cubelet.

(viii) *Mass spectrum.* We extract the mass spectrum from the restored image using a circular aperture of radius  $20''$  (denoted as A) using:

$$\frac{M_A(v_{\text{grid}})}{M_{\odot} \text{ beam}^{-1} \text{ channel}^{-1}} = \frac{\sum_A M_{ij}(v_{\text{grid}})}{\sum_A G_{ij}(v_{\text{grid}})}, \quad (8)$$

where  $G_{ij}$  represents the pixel values from the Gaussian restoring beam cubelet.

Whilst it would be possible, we decided not to stack our galaxy sample on the same physical scale, but rather chose to stack based on the same angular resolution (i.e. the  $2'' \times 2''$  being used for each pixel.). As we are only interested in recovering total H I mass in this work, stacking on the same physical scale is not required, and stacking on the same angular scale will limit the point spread function variance and hence enhance the chances of successful deconvolution.

### 3.3 Results and Error Analysis

Fig. 6 shows the stacked image before and after the deconvolution for the case of distance index  $\gamma = -1$ . The restoring beam, derived from a fit to the stacked PSF cubelet, is  $16'' \times 12''$ . The image quality is considerably improved after deconvolution. As indicated in Paper I, the good image quality results from the better uv coverage achieved in the PSF stacking process (due to increased hour angle coverage), and the fact that there exists a strong source suitable for deconvolution. This is not possible before stacking.

Mass spectra are extracted using Eq. 8, and a constant baseline is then fit to the spectra. The final stacked, deconvolved and extracted spectra for  $\gamma = 0, -1, -2, -3$  are shown in Fig. 7. An integration interval of 49 channels centered on H I restframe frequency is used to derive the total H I mass from the stacked spectra. It equals to 3.0625 MHz and is conservatively wide enough to enclose the stacked signals. Errors in total H I mass are obtained from jackknife sampling (Efron 1982), using 20 jackknife re-samples of the 5442 cubelets for each value of  $\gamma$ , followed by a repeat of the stacking and deconvolution procedure.

The re-sampled spectra are fit with Gaussian functions, which are used to derive jackknife errors, and peak and integrated signal-to-noise ratios, respectively. Table 1 summarises our results. The average H I mass decreases with decreasing  $\gamma$ . This is expected, as smaller values of  $\gamma$  highlight nearby sub-samples, which include relatively low gas mass galaxies compared to distant sub-samples. The integrated S/N ratio from Table 1 is plotted as a function of

$\gamma$  in Fig. 8. S/N ratio increases from 24.3 to 46.7 for values from  $\gamma = 0$  to  $\gamma = -3$ , respectively.

However, the effective sample size – defined as  $\eta = \sum_l w_l / \max(w)$  – drops dramatically when nearby galaxies are highly weighted. With no distance weighting ( $\gamma = 0$ ), the galaxy sample size is 3622 (only image noise in the observed frame is taken into account), whereas  $\gamma = -3$  results in an effective sample size of  $\eta \sim 20$ , representing a significant increase in Poisson error and cosmic variance. Values of  $\gamma = 0$  (no distant-dependent weighting, large cosmic volume) and  $\gamma = -1$  (higher S/N ratio) are commonly seen in the literature (Delhaize et al. 2013; Rhee et al. 2013, 2016, 2018; Hu et al. 2019).

Cosmic variance errors are further investigated by investigating four of the GAMA survey regions: G02, G09, G12 and G15 (Baldry et al. 2018). These four fields have  $r$ -band magnitude limits of 19.8, 19.0, 19.0, 19.8, respectively and sky areas of  $\sim 60 \text{ deg}^2$  (except G02, with  $\sim 55.7 \text{ deg}^2$ ). Our DINGO-VLA tiles have total coverage of  $\sim 38 \text{ deg}^2$ , or a comoving volume of  $\sim 1.620 \times 10^7 \text{ Mpc}^3$ . Within each of the 4 GAMA fields we extract two rectangular regions, as defined in Table 2. In each of these 8 sub-fields we define the GAMA sub-samples with  $NQ > 2$ ,  $z < 0.095$  and  $r < 19.0$ . The resultant sample size is also listed in Table 2. We calculate total weights  $\sum D_L^{\gamma}$  for each region. The cosmic variance (the ratio of the standard deviation to the average value for the 8 sub-fields) is: 29%, 30%, 53%, and 80% for  $\gamma = 0, -1, -2, -3$ , respectively. This again shows the increasing effect of cosmic variance with decreasing values of  $\gamma$ .

For our final analysis, we use  $\gamma = -1$ . As shown above, the cosmic variance is likely to be very similar to that for  $\gamma = 0$ , but the S/N ratio of the mass estimate is improved by  $\sim 23\%$  (Table 1). With this value, the average mass is  $M_{\text{HI}} = (1.674 \pm 0.183) \times 10^9 M_{\odot}$ . However, to continue to judge likely effects arising from cosmic variance and other systematic effects, we continue to explore variation with  $\gamma$ .

## 4 COSMIC H I DENSITY $\Omega_{\text{HI}}$

### 4.1 Method 1: completeness correction

The H I mass derived above can now be used to derive the corresponding H I mass density ( $\rho_{\text{HI}}$ ). A straightforward way is to divide the  $M_{\text{HI}}$  with the volume in which the observations were carried out. Unfortunately, our parent sample is not volume-limited. We thus adopt a method previously used to measure H I density from H I stacking experiments, which is to multiply the derived H I mass to optical light ratio  $M_{\text{HI}}/L$  with the optical luminosity density (e.g. Delhaize et al. 2013; Rhee et al. 2013). In the redshift range of our stacking experiment, the GAMA survey has high completeness in most of their surveyed optical bands, and a much larger sky coverage than the area investigated here. We focus on  $r$ -band data, because it provides one of the best luminosity density estimates, and has high target completeness and redshift success rates. To convert the measured H I mass to H I mass density ( $\rho_{\text{HI}}$ ) we use:

$$\rho_{\text{HI}}' = \frac{\langle M_{\text{HI}} \rangle}{\langle L_r \rangle} \rho_r. \quad (9)$$

However, the H I mass-to-light ratio depends on luminosity and since, GAMA is a magnitude limited survey,  $\rho_{\text{HI}}$  will be potentially over-influenced by bright, relatively low  $M_{\text{HI}}/L$  galaxies. This is straightforward to deal with by assuming a power-law rela-

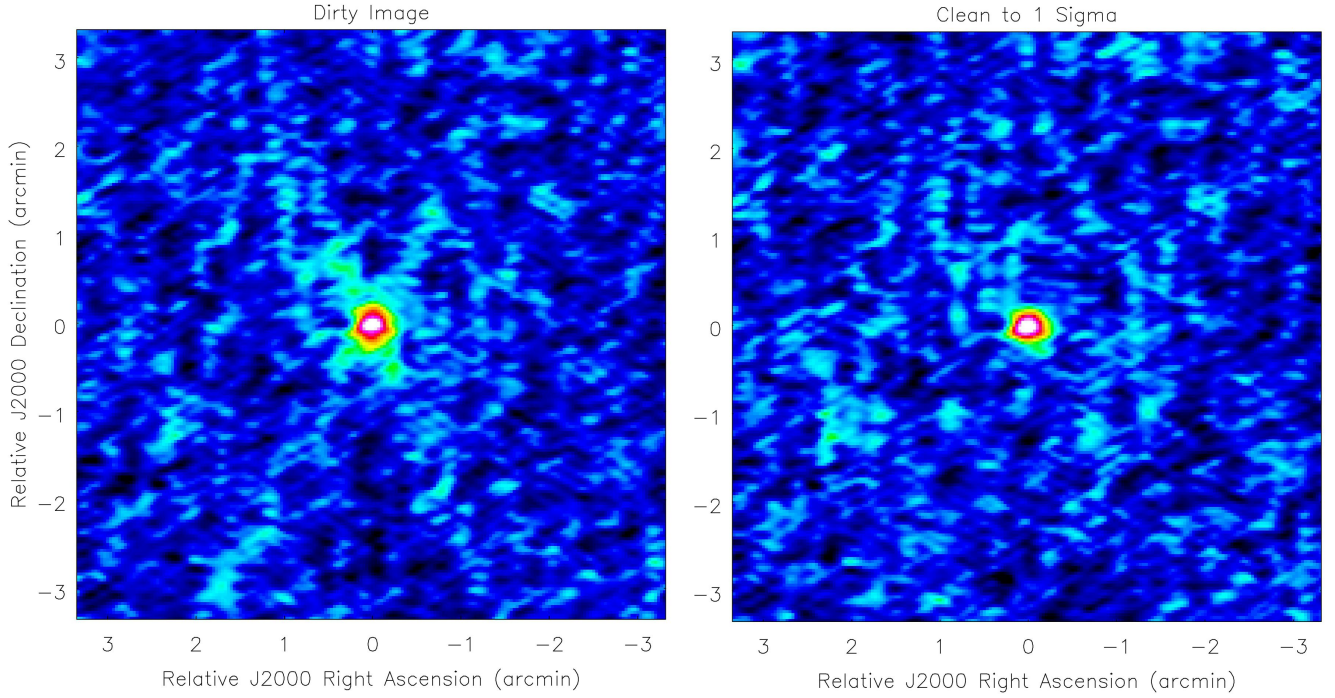


**Figure 6.** Example images of the stacked H I signal, integrated across a bandwidth of 3.0625 MHz, before and after deconvolution. Left: the moment 0 stacked image of 5442 cubelets before deconvolution. Right: the same image after deconvolving the stacked cubelet to a 1- $\sigma$  CLEAN threshold. Sidelobes are effectively suppressed by deconvolution. A weight parameter  $\gamma = -1$  is used.

**Table 1.** Final results after stacking, deconvolution and jackknife error analysis. An aperture radius of 20'' is used to extract masses. Column 1 is the weighting index; columns 2-4 are the weighted averaged redshift,  $r$ -band luminosity and measured H I mass, respectively; columns 5 and 6 are the integrated and peak S/N ratios of the extracted mass spectrum; column 7 is the completeness factor for cosmic H I density; column 8 is the derived H I cosmic density.

$\gamma$	$\langle z \rangle$	$\langle L_r \rangle$ ( $10^9 L_\odot$ )	$\langle M_{\text{H I}} \rangle$ ( $10^9 M_\odot$ )	Integrated SNR	Peak SNR	$f$	$\Omega_{\text{H I}}$ ( $10^{-3}$ )
(1)	(2)	(3)	(4)	(5)	(6)	(7)	(8)
0	0.063	6.737	$1.981 \pm 0.241$	24.3	11.7	1.442	$0.382 \pm 0.045$
-1	0.051	5.607	$1.674 \pm 0.183$	29.9	14.6	1.400	$0.377 \pm 0.042$
-2	0.035	3.718	$1.163 \pm 0.129$	39.3	20.1	1.290	$0.364 \pm 0.041$
-3	0.020	1.851	$0.626 \pm 0.110$	46.7	27.1	1.075	$0.329 \pm 0.058$

**Table 2.** Eight sub-fields defined from GAMA survey regions in order to investigate cosmic variance. Two 38 deg<sup>2</sup> regions are chosen from each of the G02, G09, G12, and G15 regions (G23 does not have the similar  $r$ -band completeness).

Region	RA (deg)	Declination (deg)	Galaxy counts
G02-1	30.2 ~ 38.8	-10.25 ~ -5.83	1733
G02-2	30.2 ~ 38.8	-8.14 ~ -3.72	3016
G09-1	129 ~ 136.6	-2 ~ 3	3460
G09-2	133.4 ~ 141	-2 ~ 3	3130
G12-1	174 ~ 181.6	-3 ~ 2	5203
G12-2	178.4 ~ 186	-3 ~ 2	4853
G15-1	211.5 ~ 219.1	-2 ~ 3	4885
G15-2	215.9 ~ 223.5	-2 ~ 3	3844

relationship between the mass-to-light ratio and luminosity:

$$\frac{M_{\text{H I}}}{L_r} = 10^{\kappa} L_r^{\beta}. \quad (10)$$

We also assume that the overall luminosity distribution is described by a Schechter function:

$$\phi(L)dL = \phi^* \left( \frac{L}{L^*} \right)^{\alpha} \exp\left(-\frac{L}{L^*}\right) \frac{dL}{L}. \quad (11)$$

A completeness correction factor can then be determined to adjust for the expected ratio between  $M_{\text{H I}}/L_r$  for the total sample and the observed sample (see Appendix A in Rhee et al. (2013)):

$$\begin{aligned} f &= \frac{\langle M_{\text{H I}} \rangle_{\text{all}} / \langle L_r \rangle_{\text{all}}}{\langle M_{\text{H I}} \rangle_{\text{obs}} / \langle L_r \rangle_{\text{obs}}} \\ &= \frac{\int_0^{\infty} L^{\beta+1} \phi(L) dL}{\int_0^{\infty} L \phi(L) dL} \frac{\int_0^{\infty} LN(L) dL}{\int_0^{\infty} L^{\beta+1} N(L) dL} \\ &= \frac{L^{\beta} \Gamma(2 + \alpha + \beta)}{\Gamma(2 + \alpha)} \frac{N}{\int_0^{\infty} L^{\beta+1} N(L) dL}, \end{aligned} \quad (12)$$

where  $\Gamma$  is the complete gamma function. We can then obtain an H I



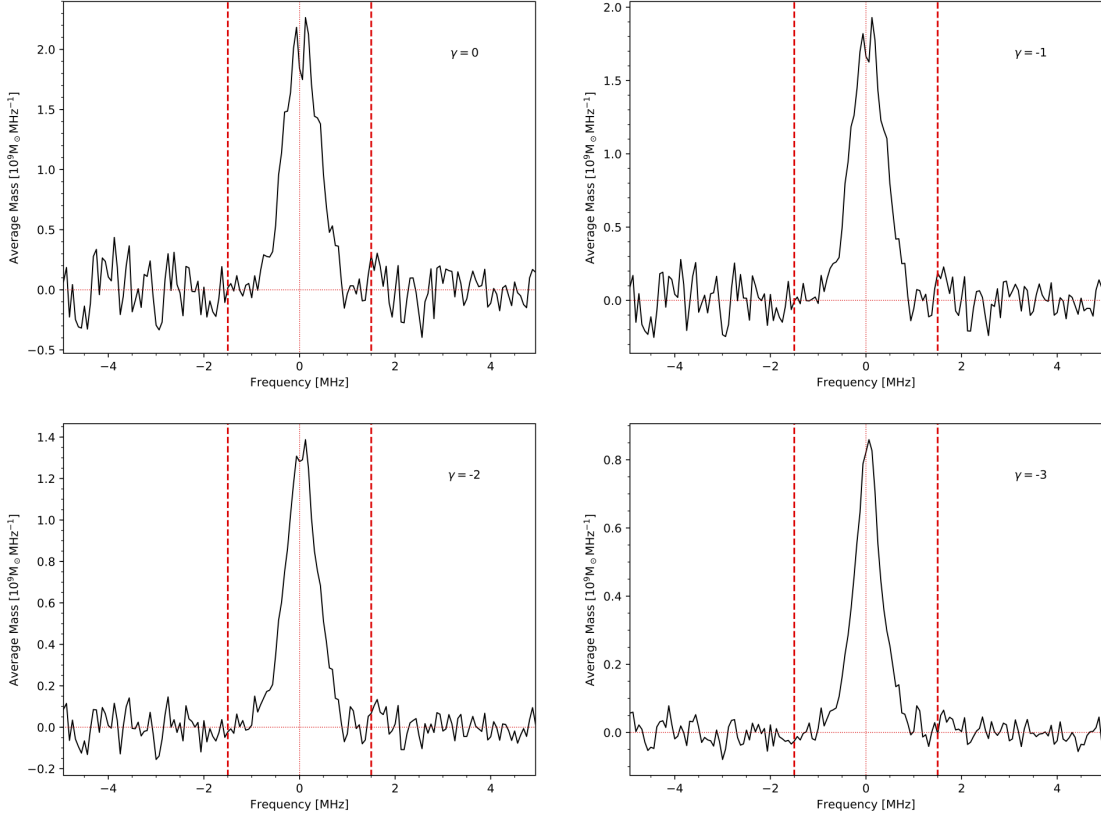


**Figure 7.** Stacked mass spectra extracted from the deconvolved cubelets for four different values of the weighting parameter,  $\gamma$ . The aperture radius used is  $R = 20''$ . The horizontal axis is centred on the H I rest-frame frequency. The vertical axis is the stacked H I mass per frequency interval. The two dashed vertical lines enclose the central 33 channels (3.0625 MHz) which are used for deriving the total H I mass. The average mass decreases for lower values of  $\gamma$ , consistent with expectation for a magnitude/flux-limited sample when bright distant galaxies are down-weighted.

density by applying this correction factor to Eq. 9 as follows:

$$\rho_{\text{HI}} = \rho'_{\text{HI}} f = \frac{\langle M_{\text{HI}} \rangle}{\langle L_r \rangle} \rho_r f, \quad (13)$$

where  $\langle M_{\text{HI}} \rangle$  is the stacked H I mass. The stacked  $r$ -band luminosity  $\langle L_r \rangle$  is calculated using the same weights as for  $\langle M_{\text{HI}} \rangle$ , but choosing the median value of  $\sigma_i$  as the noise weighting factor for each cubelet. We adopted  $\beta = -0.4$  as used in Rhee et al. (2013).

Loveday et al. (2012) studied the  $u, g, r, i, z$  luminosity functions of GAMA. We adopt their  $r$ -band low-redshift ( $z < 0.1$ ) luminosity function, with Schechter parameters from their table 3:

$$\alpha = -1.26; M_\star = -21.50; \rho_r = 1.225 \times 10^8 L_\odot \text{ Mpc}^{-3}, \quad (14)$$

where  $M_\star$  corresponds to  $L_\star = 2.88 \times 10^{10} L_\odot$  (Willmer 2018). We then calculate corresponding correction factors and cosmic H I densities from Equations 12 and 13 for different values of the weighting parameter  $\gamma$ . The cosmic H I density parameter ( $\Omega_{\text{HI}}$ ) is defined as:

$$\Omega_{\text{HI}} = \frac{\rho_{\text{HI}}}{\rho_{\text{crit},0}} = \frac{8\pi G \rho_{\text{HI}}}{3H_0^2}, \quad (15)$$

where the critical density at  $z = 0$  is defined as  $\rho_{\text{crit},0} = 1.36 \times 10^{11} M_\odot \text{ Mpc}^{-3}$ .

The results for  $\Omega_{\text{HI}}$  are summarised in Table 1. The uncertainties come from the jackknife re-sampling method described in Section 3.3.

With our preferred distance weighting index  $\gamma = -1$ , the stacked H I mass is  $(1.674 \pm 0.183) \times 10^9 M_\odot$ , resulting in a stacked mass-to-light ratio of  $(0.299 \pm 0.033) M_\odot / L_\odot$ . The derived cosmic density is  $(0.377 \pm 0.042) \times 10^{-3}$ . The VLA has an excellent flux scale accuracy to 3%-5% (Perley & Butler 2017). The errors reported are thus from jackknife analysis combined with an additional 5% assumed as the fluxscale uncertainty. We plot our result in Fig. 9, together with other results. Our result is consistent with other work in this redshift range, but with high formal accuracy.

## 4.2 Method 2: luminosity bins

We can also directly measure  $\langle M_{\text{HI}} \rangle / \langle L_r \rangle$  as a function of  $\langle L \rangle$  and extrapolate on to the universal galaxy luminosity function. We split our sample into six luminosity bins. With more than six, the stacked

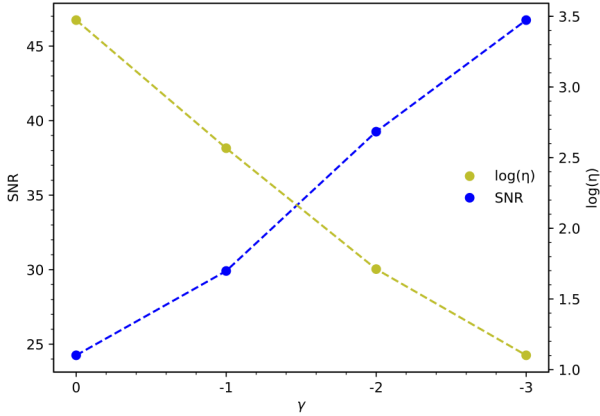


**Figure 8.** S/N ratio for the stacked H I mass measurement and the effective sample size  $\eta$ , as a function of the distance weighting factor  $\gamma$ . With lower values of  $\gamma$ , the S/N ratio increases but the effect of low sample size (and cosmic variance) becomes more significant. The effective sample size is 3622 without distance weighting ( $\eta = 0$ ), but drops to  $\sim 20$  for  $\gamma = -3$ .

**Table 3.** Number of  $z < 0.1$  DINGO-VLA galaxies, and number of cubelets for six  $r$ -band luminosity bins.

Bin	$N_{\text{gal}}$	$N_{\text{cubelets}}$	Luminosity Range ( $10^9 L_{\odot}$ )
1	600	894	0.02 ~ 0.86
2	600	895	0.86 ~ 1.62
3	600	901	1.62 ~ 2.76
4	600	901	2.76 ~ 5.07
5	600	912	5.07 ~ 11.44
6	622	939	11.45 ~ 159.57

PSFs become less stable, and the S/N ratio becomes too small. The luminosity range and number counts of galaxies and cubelets for the six bins is shown in Table 3.

For these six bins, we implement the above stacking and deconvolution procedure, and derive the stacked spectra. A constant frequency integration width of 3.0625 MHz is retained. The H I density can then be measured without any correction factor as:

$$\rho_{\text{HI}} = \int_{L_{\text{min}}}^{\infty} M_{\text{HI}}(L)\phi(L)dL, \quad (16)$$

where  $\phi(L)$  is the standard Schechter function. To better extrapolate to lower masses, we can also assume a power law relation  $M_{\text{HI}}/L \sim L^{\beta}$ , and solve for  $\kappa$  and  $\beta$  in:

$$\log_{10} \frac{\langle M_{\text{HI}} \rangle}{\langle L_r \rangle} = \kappa + \beta \log_{10} \langle L_r \rangle. \quad (17)$$

The results are shown in Table 4. It suggests that the slope of  $\beta$  is steeper than the  $-0.4$  used previously (more negative), and therefore that the contribution from optically-faint galaxies will be significant. It also means that the contribution of low-mass galaxies to the cosmic H I density could be very significant if the slope of the HI mass function steepens, or even if it remains constant at low masses. For the time being, we only calculate the contribution of galaxies with  $L_r > 10^7 L_{\odot}$ . By using  $L_{\text{min}} = 10^7 L_{\odot}$  in Eq. 16 and

combining with Equations 11 and 17, we calculate:

$$\rho_{\text{HI}} = 10^{\kappa} \phi^{\beta+1} \gamma_{\text{up}} \left( \alpha + \beta + 2, \frac{L_{\text{low}}}{L_{\star}} \right) M_{\odot} \text{ Mpc}^{-3}, \quad (18)$$

where  $\gamma_{\text{up}}$  is the upper incomplete gamma function, defined as

$$\gamma_{\text{up}}(\xi, \theta) = \int_{\theta}^{\infty} t^{\xi-1} e^{-t} dt. \quad (19)$$

The results for  $\Omega_{\text{HI}}$  are shown in Table 4. The uncertainties come from jackknife re-sampling, with 10 jackknife re-samples combined with 5% fluxscale error. The integrated and peak S/N are calculated in the same manner as in Table 1. The derived values for  $\Omega_{\text{HI}}$  are all slightly larger compared to method 1, but with excellent overall agreement. However, this method relies on successful parameter fit of  $\kappa$  and  $\beta$ , which requires accurate  $M_{\text{HI}}$  measurements in the six stacking sub-samples. This makes it less certain than the first method. We formally prefer the  $\gamma = -1$  value of  $\Omega_{\text{HI}} = (0.377 \pm 0.042) \times 10^{-3}$  in Table 1.

## 5 SUMMARY AND CONCLUSION

We have applied a new *Cubelet Stacking* technique to the  $z < 0.1$  data from the DINGO-VLA survey using a pipeline developed specifically to cope with large survey data. As the H I signals from the sample galaxies are weak and potentially resolved by the interferometer, the traditional stacking method does not work particularly well, and leads to large flux errors. We therefore stacked image and PSF cubes and deconvolved the resultant detections. This is not possible in normal H I spectral stacking. Using this method, 5442 cubelets from 3622 galaxies are stacked, then the resultant cube was deconvolved. As shown in Paper I, a deep  $1\text{-}\sigma$  threshold CLEAN and a aperture radius of  $R = 20''$  results in the most accurate stacked spectrum. We investigate different sample weighting schemes ( $w = \sigma^{-2} D^{\gamma}$ ) and find that  $\gamma = -1$  is the best compromise, giving good S/N ratio results for the stacked data and low cosmic variance. We make a  $30\sigma$  measurement of the stacked H I mass for our sample,  $\langle M_{\text{HI}} \rangle = (1.674 \pm 0.183) \times 10^9 M_{\odot}$ . The corresponding cosmic density is  $\Omega_{\text{HI}} = (0.377 \pm 0.042) \times 10^{-3}$  at  $z \sim 0.051$ . We also directly measure the cosmic H I density in six independent luminosity bins and obtain results in good agreement. All data points in Fig. 9 have been adjusted to the 737 cosmology framework (i.e.,  $H_0 = 70 \text{ km s}^{-1} \text{ Mpc}^{-1}$ ,  $\Omega_{\text{M}}=0.3$ ,  $\Omega_{\Lambda}=0.7$ ). We should note that we assume that the H I is optical thin, and that self-absorption is negligible. Previous work on nearby galaxies suggests that corrections of the order of 10s of per cent may be required (Stanimirovic et al. 1999; Liu et al. 2019). Systematic errors may also arise from incomplete optical spectroscopy. However, the G09 data being used in this work has an overall completeness of 98.48% at  $r < 19.8$ , so incompleteness down to this limit should not affect our measurements. Finally, the DINGO-VLA data analysed in this work occupies  $\sim 38 \text{ deg}^2$  equatorial area with redshift spans from 0.002 to 0.1. The cosmic variance in this region is as large as 27.05%.<sup>2</sup> The  $r$ -band luminosity density used in this paper is generated from multiple GAMA regions, and the overall cosmic variance in GAMA is less than 10% (Driver & Robotham 2010). But still, this is the an important uncertainty source in this work.

Including our work, measurements of cosmic HI density beneath  $z \sim 0.4$  largely agree with each other (see Fig. 9). These results indicate that  $\Omega_{\text{HI}}$  has not evolved significantly of the past

<sup>2</sup> From <https://cosmocalc.icrar.org>.

**Table 4.** Results derived from stacking six luminosity sub-samples. Column 1 is weighting index  $\gamma$ ; column 2 is the luminosity bin number; columns 3 to 5 are the weighting averaged redshift,  $r$ -band luminosity and the derived H I mass values, respectively; columns 6 and 7 are the integrated and peak S/N ratios for the extracted spectra, respectively; columns 8 and 9 are the parameter fits from Eq. 17

$\gamma$	Bin	$\langle z \rangle$	$\langle L_r \rangle$ ( $10^9 L_\odot$ )	$\langle M_{\text{HI}} \rangle$ ( $10^9 M_\odot$ )	Integrated SNR	Peak SNR	$\beta$	$\kappa$	$\Omega_{\text{HI}}$ ( $10^{-3}$ )
(1)	(2)	(3)	(4)	(5)	(6)	(7)	(8)	(9)	(10)
0	1	0.0401	0.475	$0.716 \pm 0.148$	8.76	8.04	-0.528	4.735	0.465
	2	0.0635	1.237	$0.621 \pm 0.316$	3.55	4.37			
	3	0.0690	2.128	$1.646 \pm 0.481$	8.27	5.16			
	4	0.0698	3.804	$2.831 \pm 0.506$	11.94	5.16			
	5	0.0690	7.696	$2.959 \pm 0.645$	12.63	5.67			
	6	0.0685	25.508	$3.408 \pm 0.762$	16.67	4.97			
-1	1	0.0309	0.383	$0.583 \pm 0.084$	11.73	10.59	-0.529	4.740	0.455
	2	0.0571	1.219	$0.680 \pm 0.274$	4.84	5.17			
	3	0.0607	2.122	$1.648 \pm 0.405$	10.71	6.68			
	4	0.0615	3.813	$2.603 \pm 0.430$	14.03	6.11			
	5	0.0626	7.746	$2.908 \pm 0.526$	15.44	6.83			
	6	0.0624	25.469	$3.246 \pm 0.637$	19.36	5.79			
-2	1	0.0214	0.283	$0.423 \pm 0.045$	17.33	15.48	-0.516	4.586	0.409
	2	0.0471	1.191	$0.726 \pm 0.222$	6.75	6.41			
	3	0.0465	2.107	$1.566 \pm 0.307$	14.59	9.14			
	4	0.0475	3.829	$2.162 \pm 0.339$	18.36	8.40			
	5	0.0538	7.828	$2.825 \pm 0.413$	19.35	8.30			
	6	0.0546	25.160	$3.030 \pm 0.523$	22.44	6.79			
-3	1	0.0144	0.201	$0.284 \pm 0.049$	22.60	20.54	-0.497	4.340	0.339
	2	0.0339	1.150	$0.736 \pm 0.171$	9.54	8.30			
	3	0.0298	2.081	$1.316 \pm 0.226$	18.52	12.28			
	4	0.0303	3.865	$1.536 \pm 0.380$	27.19	14.10			
	5	0.0433	7.935	$2.667 \pm 0.341$	22.97	9.37			
	6	0.0451	24.635	$2.732 \pm 0.449$	25.73	7.97			

$\sim 4$  Gyr. However, at higher redshifts,  $\Omega_{\text{HI}}$  shows a significant increase, especially for those measurements at  $z > 2$  using DLAs. We conduct a simple linear fit in redshift of all these measurements, weighted by their uncertainties. We show the fitting result by the dashed blue line, with the shaded region indicating the 95% confidence interval. However, it is known that theory cannot yet fully explain this evolution, possibly due to incomplete understanding of the complex physical situations which determine the boundaries between different gas phases. Predictions from semi-analytical models (such as Lagos et al. 2011, 2014, 2018; Popping et al. 2014; Kim et al. 2015; Power et al. 2010) often agree well with observations at low redshift, but at  $z > 0.4$  they show considerable discrepancies. Davé et al. (2017) uses the hydrodynamical simulation MUFASA and derives a evolution trend of  $\Omega_{\text{HI}} = 10^{-3.45}(1+z)^{0.74}$ . This model is in excellent agreement with observation results shown in Fig 9. We show this curve as the dashed orange line.

The  $\Omega_{\text{HI}}$  measurements based on 21 cm emission lines mostly cluster at  $z < 0.2$ . Our future work will examine the higher redshift portion of the DINGO-VLA data, which will provide a measurement of stacked H I content to  $z \sim 0.3$ , and contribute to the robust study of  $\Omega_{\text{HI}}$  over longer cosmological baselines. Moreover, by stacking the input GAMA galaxy sample into bins of stellar mass, colour and environment (group, cluster etc), the DINGO-VLA dataset will enable studies of gas scaling relations, gas depletion and the environmental effects on galaxy evolution. This developed cubelet stacking methodology will also be particularly useful for H I size related studies. Our future work will examine the higher redshift portion of the DINGO-VLA data (see Fig. 9) which will al-

low these studies to examine the evolution of these quantities over cosmic time.

## ACKNOWLEDGEMENTS

Parts of this research were supported by the Australian Research Council Centres of Excellence for All Sky Astrophysics in 3 Dimensions (ASTRO 3D) and All-sky Astrophysics (CAASTRO), through project numbers CE170100013 and CE110001020, respectively. Chen acknowledges Dr. Barbara Catinella, Dr. Jonghwan Rhee and Dr. Wenkai Hu for helpful discussions. The National Radio Astronomy Observatory is a facility of the National Science Foundation operated under cooperative agreement by Associated Universities, Inc.

## DATA AVAILABILITY

The raw DINGO-VLA data is available from the on-line NRAO data archive<sup>3</sup> under projects VLA/14B-315 and VLA/16A-341. The optical data for the GAMA G09 field is available from the project website<sup>4</sup>. The derived data supporting the findings of this study are available from the corresponding author on reasonable request.

<sup>3</sup> science.nrao.edu/facilities/vla/archive

<sup>4</sup> www.gama-survey.org

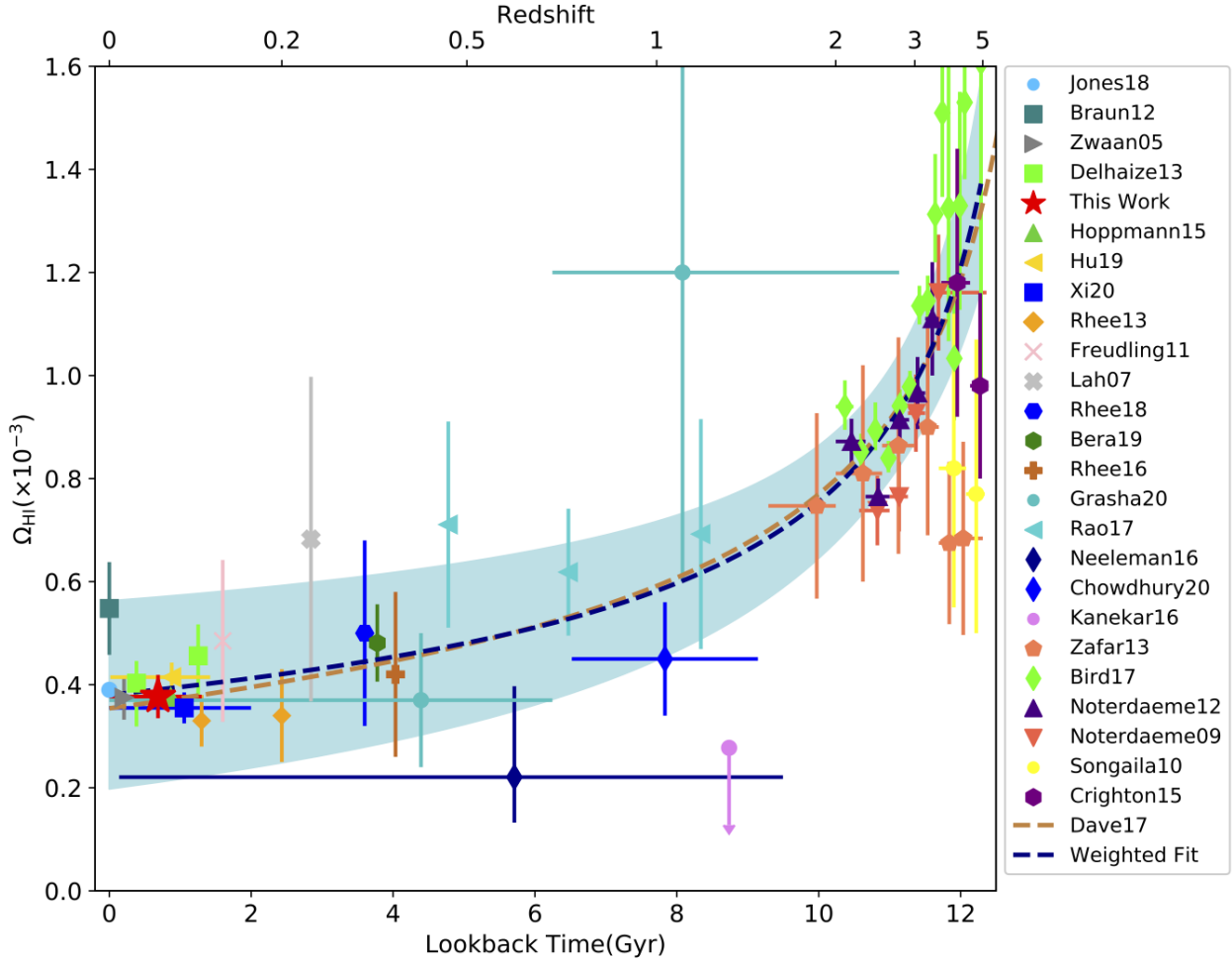


**Figure 9.** The cosmic neutral hydrogen density  $\Omega_{\text{H I}}$  plotted as a function of redshift and lookback time. The sources for the measurements are noted in the right-hand legend, sorted by redshift. All measurements are corrected to the cosmology used here. Similarly, DLA measurements which add other components (Helium, molecules) are corrected back to H I only. [Braun \(2012\)](#) analysed the H I absorption in nearby galaxies and applied an opacity correction; the [Jones et al. \(2018\)](#) measurement is from the ALFALFA 100% survey; [Delhaize et al. \(2013\)](#) has data points from two Parkes studies: HIPASS and a deep observation towards the south galactic pole; the result presented here is plotted as the red star; [Freudling et al. \(2011\)](#), [Hoppmann et al. \(2015\)](#) and [Xi et al. \(2020\)](#) are direct detection measurements from the Arecibo Ultra Deep Survey (AUDS); [Rhee et al. \(2013\)](#) and [Hu et al. \(2019\)](#) are both H I stacking experiments using the WSRT; [Zwaan et al. \(2005\)](#) is the HIPASS measurement; [Lah et al. \(2007\)](#), [Rhee et al. \(2016\)](#) and [Rhee et al. \(2018\)](#) use stacked GMRT 21-cm emission-line data; [Bera et al. \(2019\)](#) is also a spectral stacking measurement using GMRT 21-cm emission data; the two [Grasha et al. \(2020\)](#) measurements are from DLA data from the Green Bank Telescope (GBT); [Rao et al. \(2017\)](#) is a DLA measurement based on a sample of MgII absorbers; [Neeleman et al. \(2016\)](#) is a DLA measurement based on HST archival UV data; [Chowdhury et al. \(2020\)](#) is an H I stacking experiment using GMRT; the [Kanekar et al. \(2016\)](#) upper limit is from stacked GMRT H I emission-line data for bright star forming galaxies; [Zafar et al. \(2013\)](#) quotes DLA measurements from ESO UVES; [Noterdaeme et al. \(2009\)](#), [Noterdaeme et al. \(2012\)](#), [Bird et al. \(2017\)](#) are DLA analyses using SDSS DR7, DR9 and DR12, respectively; [Songaila & Cowie \(2010\)](#) provide DLA measurements from Keck data; [Crighton et al. \(2015\)](#) quote results from a Gemini GMOS study of DLAs. The dashed light orange line is from the [Davé et al. \(2017\)](#) model; the dashed navy blue line is a weighted linear fit to all the available measurements, with the shaded region representing the 95% confidence region.

## REFERENCES

- Ahn C. P., et al., 2014, *ApJS*, **211**, 17  
 Baldry I. K., et al., 2014, *MNRAS*, **441**, 2440  
 Baldry I. K., et al., 2018, *MNRAS*, **474**, 3875  
 Bera A., Kanekar N., Chengalur J. N., Bagla J. S., 2019, *ApJ*, **882**, L7  
 Bird S., Garnett R., Ho S., 2017, *MNRAS*, **466**, 2111  
 Braun R., 2012, *ApJ*, **749**, 87  
 Briggs D. S., 1995, in American Astronomical Society Meeting Abstracts. p. 112.02  
 Cannon R., et al., 2006, *MNRAS*, **372**, 425  
 Carilli C. L., Rawlings S., 2004, *New Astron. Rev.*, **48**, 979  
 Cen R., Ostriker J. P., Prochaska J. X., Wolfe A. M., 2003, *ApJ*, **598**, 741  
 Chen Q., Meyer M., Popping A., Staveley-Smith L., 2021, *MNRAS*, **502**, 2308  
 Chengalur J. N., Braun R., Wieringa M., 2001, *Astronomy & Astrophysics*, **372**, 768  
 Chowdhury A., Kanekar N., Chengalur J. N., Sethi S., Dwarakanath K. S., 2020, *Nature*, **586**, 369  
 Crighton N. H. M., et al., 2015, *MNRAS*, **452**, 217



- Croom S. M., et al., 2009, *MNRAS*, **392**, 19
- Davé R., Rafieferantsoa M. H., Thompson R. J., Hopkins P. F., 2017, *MNRAS*, **467**, 115
- DeBoer D. R., et al., 2009, *IEEE Proceedings*, **97**, 1507
- Delhaize J., Meyer M. J., Staveley-Smith L., Boyle B. J., 2013, *MNRAS*, **433**, 1398
- Driver S. P., Robotham A. S. G., 2010, *MNRAS*, **407**, 2131
- Driver S. P., et al., 2011, *MNRAS*, **413**, 971
- Efron B., 1982, The Jackknife, the Bootstrap and other resampling plans
- Ellison S. L., Yan L., Hook I. M., Pettini M., Wall J. V., Shaver P., 2001, *A&A*, **379**, 393
- Falco E. E., et al., 1999, *PASP*, **111**, 438
- Fernández X., et al., 2013, *ApJ*, **770**, L29
- Fernández X., et al., 2016, *ApJ*, **824**, L1
- Freudling W., et al., 2011, *ApJ*, **727**, 40
- Giovanelli R., Haynes M. P., 2015, *A&ARv*, **24**, 1
- Giovanelli R., et al., 2005, *AJ*, **130**, 2598
- Gogate A. R., Verheijen M. A. W., Deshev B. Z., van Gorkom J. H., Montero-Castaño M., van der Hulst J. M., Jaffé Y. L., Poggianti B. M., 2020, *MNRAS*, **496**, 3531
- Grasha K., Darling J., Leroy A. K., Bolatto A. D., 2020, *MNRAS*, **498**, 883
- Hess K. M., et al., 2019, *MNRAS*, **484**, 2234
- Hopkins A. M., 2004, *ApJ*, **615**, 209
- Hopkins A. M., Beacom J. F., 2006, *The Astrophysical Journal*, **651**, 142
- Hopkins A. M., McClure-Griffiths N. M., Gaensler B. M., 2008, *ApJ*, **682**, L13
- Hopkins A. M., et al., 2013, *MNRAS*, **430**, 2047
- Hoppmann L., Staveley-Smith L., Freudling W., Zwaan M. A., Minchin R. F., Calabretta M. R., 2015, *MNRAS*, **452**, 3726
- Hu W., et al., 2019, *MNRAS*, **489**, 1619
- Jonas J. L., 2009, *IEEE Proceedings*, **97**, 1522
- Jones D. H., et al., 2009, *MNRAS*, **399**, 683
- Jones M. G., Haynes M. P., Giovanelli R., Moorman C., 2018, *MNRAS*, **477**, 2
- Jorgenson R. A., Wolfe A. M., Prochaska J. X., Lu L., Howk J. C., Cooke J., Gawiser E., Gelino D. M., 2006, *ApJ*, **646**, 730
- Kanekar N., Sethi S., Dwarakanath K. S., 2016, *ApJ*, **818**, L28
- Kim H.-S., Wyithe J. S. B., Power C., Park J., Lagos C. d. P., Baugh C. M., 2015, *MNRAS*, **453**, 2315
- Lagos C. D. P., Baugh C. M., Lacey C. G., Benson A. J., Kim H.-S., Power C., 2011, *MNRAS*, **418**, 1649
- Lagos C. D. P., Baugh C. M., Zwaan M. A., Lacey C. G., Gonzalez-Perez V., Power C., Swinbank A. M., van Kampen E., 2014, *MNRAS*, **440**, 920
- Lagos C. d. P., Tobar R. J., Robotham A. S. G., Obreschkow D., Mitchell P. D., Power C., Elahi P. J., 2018, *MNRAS*, **481**, 3573
- Lah P., et al., 2007, *MNRAS*, **376**, 1357
- Lah P., et al., 2009, *MNRAS*, **399**, 1447
- Lilly S. J., Le Fevre O., Hammer F., Crampton D., 1996, *ApJ*, **460**, L1
- Liske J., et al., 2015, *MNRAS*, **452**, 2087
- Liu B., Li D., Staveley-Smith L., Qian L., Wong T., Goldsmith P., 2019, *ApJ*, **887**, 242
- Loveday J., et al., 2012, *MNRAS*, **420**, 1239
- Madau P., Dickinson M., 2014, *ARA&A*, **52**, 415
- Madau P., Ferguson H. C., Dickinson M. E., Giavalisco M., Steidel C. C., Fruchter A., 1996, *MNRAS*, **283**, 1388
- Martin A. M., Papastergis E., Giovanelli R., Haynes M. P., Springob C. M., Stierwalt S., 2010, *ApJ*, **723**, 1359
- McMullin J. P., Waters B., Schiebel D., Young W., Golap K., 2007, in Shaw R. A., Hill F., Bell D. J., eds, *Astronomical Society of the Pacific Conference Series Vol. 376, Astronomical Data Analysis Software and Systems XVI*. p. 127
- Meyer M., 2009, in *Panoramic Radio Astronomy: Wide-field 1-2 GHz Research on Galaxy Evolution*. p. 15 ([arXiv:0912.2167](https://arxiv.org/abs/0912.2167))
- Meyer M. J., et al., 2004, *MNRAS*, **350**, 1195
- Meyer M., Robotham A., Obreschkow D., Westmeier T., Duffy A. R., Staveley-Smith L., 2017, *Publ. Astron. Soc. Australia*, **34**, 52
- Nagamine K., Cen R., Hernquist L., Ostriker J. P., Springel V., 2005, *ApJ*, **627**, 608
- Neeleman M., Prochaska J. X., Ribaud J., Lehner N., Howk J. C., Rafelski M., Kanekar N., 2016, *ApJ*, **818**, 113
- Noterdaeme P., Petitjean P., Ledoux C., Srianand R., 2009, *A&A*, **505**, 1087
- Noterdaeme P., et al., 2012, *A&A*, **547**, L1
- Parkinson D., et al., 2012, *Phys. Rev. D*, **86**, 103518
- Perley R., 2016, ELVA Memo, 195
- Perley R. A., Butler B. J., 2017, *ApJS*, **230**, 7
- Popping G., Somerville R. S., Trager S. C., 2014, *MNRAS*, **442**, 2398
- Power C., Baugh C. M., Lacey C. G., 2010, *MNRAS*, **406**, 43
- Prochaska J. X., Wolfe A. M., 2009, *ApJ*, **696**, 1543
- Prochaska J. X., Herbert-Fort S., Wolfe A. M., 2005, *ApJ*, **635**, 123
- Rao S. M., Turnshek D. A., Sardane G. M., Monier E. M., 2017, *MNRAS*, **471**, 3428
- Rau U., Cornwell T. J., 2011, *A&A*, **532**, A71
- Rhee J., Zwaan M. A., Briggs F. H., Chengalur J. N., Lah P., Oosterloo T., van der Hulst T., 2013, *MNRAS*, **435**, 2693
- Rhee J., Lah P., Chengalur J. N., Briggs F. H., Colless M., 2016, *MNRAS*, **460**, 2675
- Rhee J., Lah P., Briggs F. H., Chengalur J. N., Colless M., Willner S. P., Ashby M. L. N., Le Fevre O., 2018, *MNRAS*, **473**, 1879
- Smette A., Claeskens J.-F., Surdej J., 1997, *New Astronomy*, **2**, 53
- Somerville R. S., Primack J. R., Faber S. M., 2001, *MNRAS*, **320**, 504
- Songaila A., Cowie L. L., 2010, *ApJ*, **721**, 1448
- Stanimirovic S., Staveley-Smith L., Dickey J. M., Sault R. J., Snowden S. L., 1999, *MNRAS*, **302**, 417
- Tonry J. L., Blakeslee J. P., Ajhar E. A., Dressler A., 2000, *ApJ*, **530**, 625
- Willmer C. N. A., 2018, *ApJS*, **236**, 47
- Xi H., Staveley-Smith L., For B.-Q., Freudling W., Zwaan M., Hoppmann L., Liang F.-H., Peng B., 2020, *MNRAS*, **491**, 1000
- Zafar T., Péroux C., Popping A., Milliard B., Deharveng J.-M., Frank S., 2013, *A&A*, **556**, A141
- Zwaan M. A., 2000, PhD thesis, -
- Zwaan M. A., Meyer M. J., Staveley-Smith L., Webster R. L., 2005, *MNRAS*, **359**, L30

This paper has been typeset from a  $\text{\TeX}/\text{\LaTeX}$  file prepared by the author.